GEOPHYSICS, VOL. 53, NO. 9 (SEPTEMBER 1988); P. 1184–1193, 11 FIGS.

Three-dimensional elastic modeling by the Fourier method

Moshe Reshef*, Dan Kosloff‡, Mickey Edwards§,
and Chris Hsiung**

ABSTRACT

Earlier work on three-dimensional forward modeling is extended to elastic waves using the equations of conservation of momentum and the stress-strain relations for an isotropic elastic medium undergoing infinitesimal deformation. In addition to arbitrary compressional (or *P*-wave) velocity and density variation in lateral and vertical directions, elastic modeling permits shear (or *S*-wave) velocity variation as well. The elastic wave equation is solved using a generalization of the method for the acoustic case. Computation of each time step begins by computing six strain components by performing nine spatial partial differentiation operations on the three displacement components from the previous time step. The six strains and two Lamé constants are linearly combined to yield six stress components. Nine spatial partial differentiation operations on the six stresses, three body forces, and density are used to compute second partial time derivatives of the three displacement components. Time stepping to obtain the three displacement components for the current time step is performed with second-order difference operators. The modeling includes an optional free surface above the spatial grid. An absorbing boundary is applied on the lateral and bottom edges of the spatial grid.

This modeling scheme is implemented on a four-processor CRAY X-MP computer system using the solid-state storage device (SSD). Using parallel processing with four CPUs, a reasonable geologic model can be computed within a few hours. The modeling scheme provides a variety of seismic source types and many possible output displays. These features enable the modeling of a wide range of seismic surveys. Numerical and analytic results are presented.

INTRODUCTION

Clearly, elastic forward modeling represents a more severe challenge to computer technology than does acoustic modeling (Reshef et al., 1988, this issue). Using the Fourier method, the elastic case requires almost an order of magnitude more computations than does the acoustic case for comparable grids. Depending upon the density assumption, three or six times more fast Fourier transform (FFT) operations are required. Excluding spatial differentiation, approximately four times as many algebraic operations are required. The elastic case requires three times as many variables at each grid point. As in the acoustic case, memory requirements represent the foremost challenge. Wall-clock times would be increased by at least a factor of five if the SSD were replaced by conventional disk storage. The factor of five assumes parallel disk streaming.

Current memory technology advances and parallel processing trends and directions within the computer industry make three-dimensional (3-D) algorithms promising, including those for forward modeling. Employing more than four CPUs on the same problem reduces computational time. Major computer enhancements, such as reducing the clock period, would further reduce computational time. Current execution times of a few hours must be reduced to execution times of a few minutes for the simulation of a two-dimensional or three-dimensional field survey with a line of sources.

The following sections address the basic equations for isotropic elastic media, the Fourier numerical solution method, computer implementation, and modeling examples. The nu-

Manuscript received by the Editor December 1, 1986; revised manuscript received February 29, 1988.
*Formerly Cray Research Inc., Houston; presently Department of Geophysics and Planetary Sciences, Tel Aviv University, Tel Aviv 69978, Israel.
‡Formerly Federal University of Bahia, Salvador, Bahia, Brazil; presently Department of Geophysics and Planetary Sciences, Tel Aviv University, Tel Aviv 69978, Israel.
§Cray Research Inc., 5847 San Felipe, Ste. 3000, Houston, TX 77057.
**Cray Research Inc., 900 Lowater Road, Chippewa Falls, WI 54729.

merical solution differs from that for the two-dimensional (2-D) case (Kosloff et al., 1984; Reshef and Kosloff, 1985) in that displacements have not been eliminated from the computational equations. Numerical stability and dispersion requirements were found to be the same as in the 2-D case.

BASIC EQUATIONS

For an isotropic elastic medium undergoing infinitesimal deformation, the equations of momentum conservation are given by the following (Fung, 1965):

$$\rho\ddot{U}_x = \frac{\partial\sigma_{xx}}{\partial x} + \frac{\partial\sigma_{xy}}{\partial y} + \frac{\partial\sigma_{xz}}{\partial z} + f_x,$$

$$\rho\ddot{U}_y = \frac{\partial\sigma_{xy}}{\partial x} + \frac{\partial\sigma_{yy}}{\partial y} + \frac{\partial\sigma_{yz}}{\partial z} + f_y, \tag{1}$$

and

$$\rho\ddot{U}_z = \frac{\partial\sigma_{xz}}{\partial x} + \frac{\partial\sigma_{yz}}{\partial y} + \frac{\partial\sigma_{zz}}{\partial z} + f_z.$$

The stress components are σ_{xx}, σ_{yy}, σ_{zz}, σ_{xy}, σ_{xz}, and σ_{yz}; f_x, f_y, and f_z are the body forces; the displacement components are U_x, U_y, and U_z; $\ddot{U}_x$, $\ddot{U}_y$, and $\ddot{U}_z$ are the second partial time derivatives of displacement space (or acceleration components); and ρ denotes the density. Equations relating stress and strain components can be written as follows:

$$\begin{aligned}
\sigma_{xx} &= \lambda(e_{xx} + e_{yy} + e_{zz}) + 2\mu e_{xx},\\
\sigma_{yy} &= \lambda(e_{xx} + e_{yy} + e_{zz}) + 2\mu e_{yy},\\
\sigma_{zz} &= \lambda(e_{xx} + e_{yy} + e_{zz}) + 2\mu e_{zz},\\
\sigma_{xy} &= 2\mu e_{xy},\\
\sigma_{xz} &= 2\mu e_{xz},
\end{aligned} \tag{2}$$

and

$$\sigma_{yz} = 2\mu e_{yz}.$$

λ and μ denote the Lamé constants and e_{xx}, e_{yy}, e_{zz}, e_{xy}, e_{xz}, and e_{yz} are the body strains. Strains can be expressed in terms of displacements as follows:

$$\begin{aligned}
e_{xx} &= \frac{\partial U_x}{\partial x},\\
e_{yy} &= \frac{\partial U_y}{\partial y},\\
e_{zz} &= \frac{\partial U_z}{\partial z},\\
e_{xy} &= \frac{1}{2}\left(\frac{\partial U_x}{\partial y} + \frac{\partial U_y}{\partial x}\right),\\
e_{xz} &= \frac{1}{2}\left(\frac{\partial U_x}{\partial z} + \frac{\partial U_z}{\partial x}\right),
\end{aligned} \tag{3}$$

and

$$e_{yz} = \frac{1}{2}\left(\frac{\partial U_y}{\partial z} + \frac{\partial U_z}{\partial y}\right).$$

Lamé constants can be expressed as functions of P-wave and S-wave velocities (V_p and V_s) and density as follows:

$$\mu = \rho V_s^2,$$

and

$$\lambda = \rho(V_p^2 - 2V_s^2). \tag{4}$$

Equations (1)–(3) can be found in any fundamental development of elasticity theory. Density ρ and Lamé constants λ and μ are functions of Cartesian coordinates x, y, and z. All other terms in equations (1)–(3) are functions of x, y, z, and the time t.

Numerical solution method

At each time step, the first computation is for strains with equation (3), using displacement components from the previous time step. Computations continue with the computation of the stresses using equation (2). Finally, the second partial time derivatives of the displacement components are computed with equation (1). Spatial partial differentiation is performed by FFTs using odd-based mixed radixes. That is, the length of each FFT or the number of points along each axis is the product of the powers of odd integers. Computation with Nyquist wavenumbers is avoided. Complex FFTs use odd and even real lines or columns loaded into real and imaginary components, respectively. FFT performance is comparable to conventional radix two FFTs (Temperton, 1983).

Depending upon the type of source, stress differentiation is modified for computational efficiency. If a pressure source is used, equations (1) are rewritten as follows:

$$\rho\ddot{U}_x = \frac{\partial(\sigma_{xx} + 1/3\Phi)}{\partial x} + \frac{\partial\sigma_{xy}}{\partial y} + \frac{\partial\sigma_{xz}}{\partial z},$$

$$\rho\ddot{U}_y = \frac{\partial\sigma_{xy}}{\partial x} + \frac{\partial(\sigma_{yy} + 1/3\Phi)}{\partial y} + \frac{\partial\sigma_{yz}}{\partial z}, \tag{5}$$

and

$$\rho\ddot{U}_z = \frac{\partial\sigma_{xz}}{\partial x} + \frac{\partial\sigma_{yz}}{\partial y} + \frac{\partial(\sigma_{zz} + 1/3\Phi)}{\partial z},$$

where $\Phi(x, y, z, t)$ is a scalar potential. For a shear source with a vector potential given by

$$\mathbf{S} = \mathbf{i}S_x + \mathbf{j}S_y + \mathbf{k}S_z,$$

the body forces are equal to the curl of $\mathbf{S}$,

$$\begin{aligned}
f_x &= \frac{\partial S_z}{\partial y} - \frac{\partial S_y}{\partial z},\\
f_y &= \frac{\partial S_x}{\partial z} - \frac{\partial S_z}{\partial x},
\end{aligned} \tag{6}$$

and

$$f_z = \frac{\partial S_y}{\partial x} - \frac{\partial S_x}{\partial y}.$$

For computational efficiency, the above body forces are introduced by rewriting equations (1) as follows:

$$\begin{aligned}
\rho\ddot{U}_x &= \frac{\partial\sigma_{xx}}{\partial x} + \frac{\partial(\sigma_{xy} + S_z)}{\partial y} + \frac{\partial(\sigma_{xz} - S_y)}{\partial z},\\
\rho\ddot{U}_y &= \frac{\partial(\sigma_{xy} - S_z)}{\partial x} + \frac{\partial\sigma_{yy}}{\partial y} + \frac{\partial(\sigma_{yz} + S_x)}{\partial z},
\end{aligned} \tag{7}$$

and

$$\rho\ddot{U}_z = \frac{\partial(\sigma_{xz} + S_y)}{\partial x} + \frac{\partial(\sigma_{yz} - S_x)}{\partial y} + \frac{\partial\sigma_{zz}}{\partial z}.$$

For a directional force

$$\mathbf{F} = \mathbf{i}f_x + \mathbf{j}f_y + \mathbf{k}f_z,$$

body forces f_x, f_y, f_z are introduced according to equations (1). In all cases, separable sources are used; for example,

$$\Phi(x, y, z, t) = \Phi(x, y, z)h(t),$$

where $h(t)$ is a band-limited wavelet.

Time stepping involves computing new displacement components at the current time step by second-order differencing. We obtain new velocity and displacement components as follows:

$$\dot{U}_u\left[x, y, z, (n + \tfrac{1}{2})\Delta t\right] = \dot{U}_u\left[x, y, z, (n - \tfrac{1}{2})\Delta t\right] + \Delta t\ddot{U}_u(x, y, z, n\Delta t),$$

and (8)

$$U_u\left[x, y, z, (n + 1)\Delta t\right] = U_u(x, y, z, n\Delta t) + \Delta t\dot{U}_u\left[x, y, z, (n + \tfrac{1}{2})\Delta t\right],$$

where u stands for x, y, or z.

Following time stepping, similar to that in the acoustic case, an absorbing boundary condition is applied to the three displacements and the three first partial time derivatives of the displacements on the bottom and lateral edges of the spatial grid. The absorbing boundary condition is applied as a 15-point weighting function (Cerjan et al., 1985).

Similar to the acoustic case, for the top boundary there is an option of introducing a free surface or allowing events to wrap around to the bottom of the grid and be eliminated by the absorbing boundary. As in the 2-D case, the free-surface condition is approximated by including a wide zone with zero compressional and shear velocities above the upper surface of the model or, equivalently, because of periodicity, below the bottom of the model. Since the boundary condition is not explicitly specified, comparison with analytic solutions is required. Values of the displacement components U_x, U_y, U_z and the first time derivatives $\dot{U}_x$, $\dot{U}_y$, $\dot{U}_z$ must be saved for each coordinate of the padded or extended zone below the model.

Computer implementation

The preceding section represents a functional description of the numerical method. This section describes the numerical algorithm actually implemented. Let NX, NY, and NZ denote the number of grid points in the x, y, and z directions. The numerical solution of equations (1)–(3) requires nine global arrays of size $NX \times NY \times NZ$. These include displacements U_x, U_y, U_z, first partial time derivatives $\dot{U}_x$, $\dot{U}_y$, $\dot{U}_z$, and material parameters ρ, λ, μ. Six auxiliary arrays of the same size are required for partial or complete expressions of the six stresses. The algorithm has ordered computations in a manner requiring 15 arrays of values at each grid point. For example, a model of $225 \times 125 \times 225$ requires a minimum of 110 million words of storage. If a free surface is being used, six additional arrays of values are required for each grid point of the extended or padded region.

The data storage management scheme is based on a pencil structure as illustrated by Figure 1. This structure differs from that used in the acoustic case (Reshef et al., 1988) in the orientation direction and the size of each pencil. Within each pencil, the 15 variables are stored in consecutive memory locations; storage progresses most rapidly in the x direction, then in the z direction, and finally in the y direction. Each pencil contains four z, four y, and NX x coordinates. Within SSD storage, the upper forefront pencil is stored in the first $4 \times 4 \times NX$ words. Next, the storage progresses to the neighboring pencil in the z direction and then to the next row of pencils in the y direction. If a free surface is used, computations require a second set of pencils using 6 as opposed to 15 variables. A set of xz or xy planes can be retrieved or stored with a single input-output operation. Each operating system input-output request processes a list, or queue, of SSD word addresses. If software had been implemented using a separate operating system request for each pencil, one CPU would have had to have been dedicated for input-output operations.

At each time step, computation consists of calculating new values in all NZ xy and then in all NY xz planes. Parallel processing is achieved by allowing each of the four CPUs to operate on separate planes. An equal amount of computational work is performed by each CPU.

Before computations commence, pencil values of ρ, λ, and μ are stored and the remaining 12 variables (or 18 variables for the free-surface case) are set to zero for all grid coordinates. Zero displacements U_x, U_y, and U_z correspond to time $t = 0$. Zero first partial time derivatives $\dot{U}_x$, $\dot{U}_y$, and $\dot{U}_z$ correspond to time $t = -1/2\Delta t$. Using xz planes, an initialization step of calculating strains e_{xx}, e_{zz}, and e_{xz} and $\partial U_y/\partial x$ and $\partial U_y/\partial z$ terms in strains e_{xy} and e_{yz} is performed. The above terms reside in five auxiliary arrays on the SSD.

The various steps of the algorithm are summarized in the schematic diagram shown in Figure 2. Using xy planes, the first computational step calculates strain e_{yy} and completes expressions for strains e_{xy} and e_{yz} by calculating $\partial U_x/\partial y$ and $\partial U_z/\partial y$. Five auxiliary arrays retrieved from the SSD contain $\partial U_x/\partial x$ or e_{xx}, $1/2(\partial U_z/\partial x + \partial U_x/\partial z)$ or e_{xz}, $\partial U_y/\partial x$, $\partial U_z/\partial z$ or e_{zz}, and $\partial U_y/\partial z$. Using strains e_{xx}, e_{zz}, and e_{xz} computed by the previous xz-plane pass, we now compute the six stresses σ_{xx}, σ_{yy}, σ_{zz}, σ_{xy}, σ_{xz}, and σ_{yz}. Before storing current xy planes on the SSD, central memory arrays containing σ_{xy}, σ_{yy}, and σ_{yz} are replaced by partial derivatives with respect to y. Partial differentiation with respect to y depends upon the type of source according to equations (1), (5), or (7). Displacements U_x, U_y, and U_z used by the first computational step correspond to those of the previous time step.

Using xz planes, the second computational step calculates partial derivatives of stresses with respect to x and z to obtain the second partial time derivatives of displacement components $\ddot{U}_x$, $\ddot{U}_y$, and $\ddot{U}_z$ according to equations (1), (5), or (7). The six auxiliary arrays retrieved from the SSD contain the aforementioned stress terms. Partial derivative terms with respect to y were computed in the first computational step. We

now time step to obtain new first partial time derivative and displacement terms according to equations (8) and then apply the absorbing boundary condition. Before storing the current xz planes on the SSD, we compute strains e_{xx}, e_{zz}, and e_{xz} and incomplete terms for strains e_{xy} and e_{yz} ($\partial U_y/\partial x$ and $\partial U_y/\partial z$, respectively) for the next time step.

Output from the modeling can include a number of different variables. The two main types of display are time sections along horizontal or vertical lines and plane snapshots at specified times. Output can include P-wave and S-wave fields, displacements, stresses, and strains. For some types of output display, postmodeling processing is required. The pressure field $P(x, y, z, t)$ is calculated as

$$P = -\tfrac{1}{3}(\sigma_{xx} + \sigma_{yy} + \sigma_{zz}). \tag{9}$$

For shear waves, we chose to display in-plane and out-of-plane amplitudes. For an xz plane, in-plane shear amplitudes $S_{ip}(x, y, z, t)$ are calculated as the y component of the curl of the displacement vector,

$$S_{ip} = \frac{\partial U_x}{\partial z} - \frac{\partial U_z}{\partial x}. \tag{10}$$

Out-of-plane shear amplitudes $S_{op}(x, y, z, t)$ are calculated as

$$S_{op} = a\frac{\partial U_y}{\partial x} + b\frac{\partial U_y}{\partial z}, \tag{11}$$

where a and b are arbitrary numbers chosen for the clearest display. This separation of shear-wave amplitudes assumes real significance in the case of horizontally stratified structures and snapshot planes passing through the source location. For the above, S_{ip} and S_{op} correspond to SV-wave and SH-wave amplitudes, respectively. Similar expressions can be written for the xy and yz planes.

The bulk of the computations are FFT operations, which are highly suited for exploitation of parallel processing. For models computed to date, a sustainable rate of approximately 450 Mflops is achieved with the CRAY X-MP/48. Sustainable rates are computed by dividing the total number of floating-point operations by the elapsed or wall-clock time of the computer program in seconds.

The software is optimized for the hardware and Fortran compiler architecture by vectorizing Fortran loops, mini-

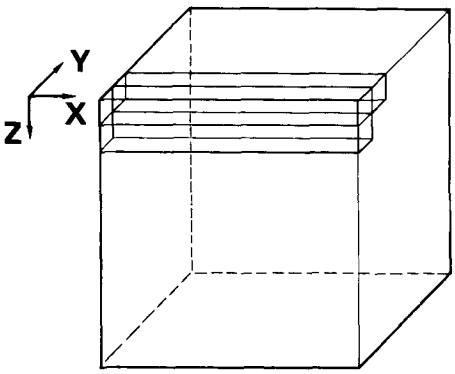

FIG. 1. Pencil data structure. Within the SSD, the upper forefront pencil is stored first. Storage progresses in the z direction and then to the next row of pencils in the y direction. Each pencil has four y, four z, and all x coordinates. Within each pencil, 15 variables (or 6 variables for the free-surface extended region) are grouped in consecutive words; x is the fastest increasing coordinate, followed by z, and then y.

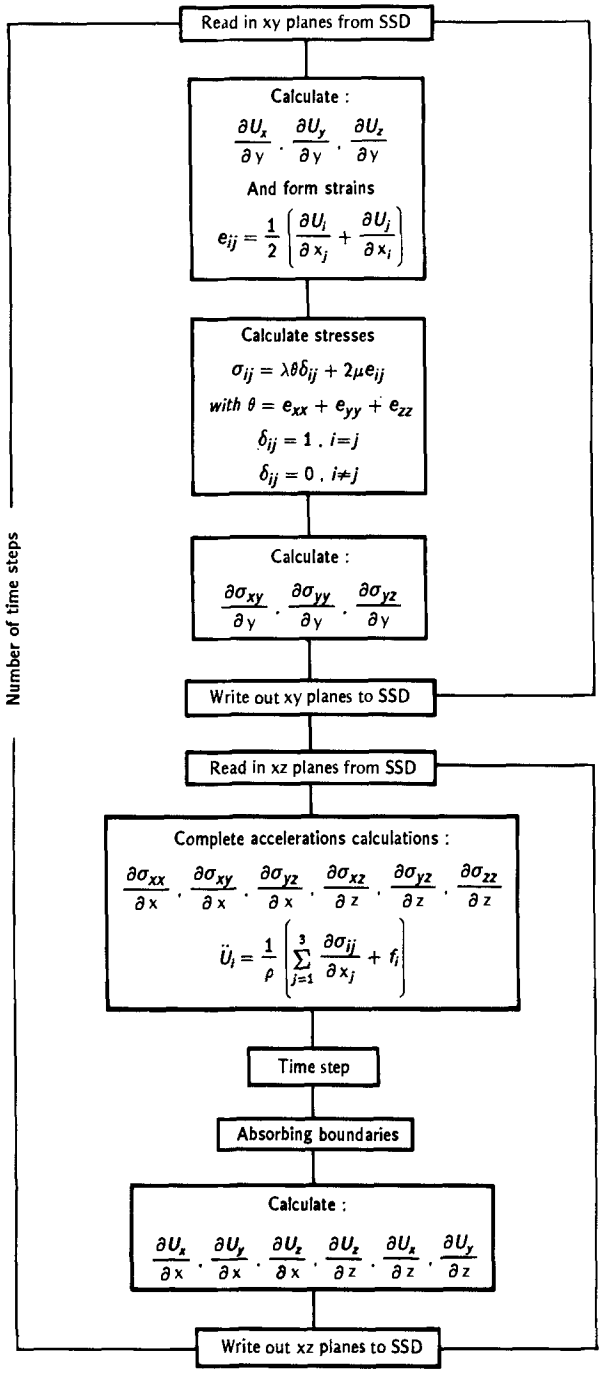

FIG. 2. Schematic diagram of algorithm steps for directional source case. For brevity, tensor notation is used in three boxes. Following computation of the last time step, partial differentiation with respect to x and z is not performed.

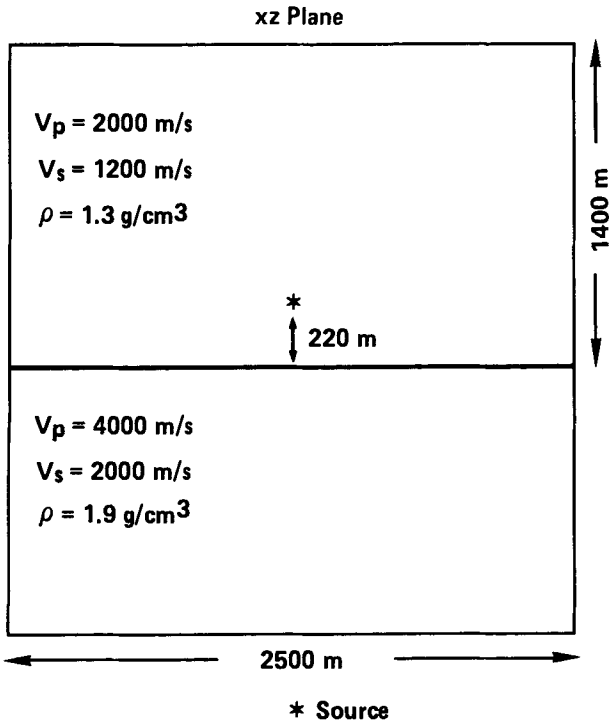

FIG. 3. Horizontal interface model—configuration and physical parameters.

mizing memory-to-memory movement or copying of data, and accessing multiplexed data with a memory increment or stride greater than one. Excluding one-time program initialization, approximately 96 percent of the computational work for each time step was distributed across the four CPUs. The remaining 4 percent of the computational work, which encompasses computations which must be performed sequentially by a single CPU, limits the degree of parallel processing which can be achieved. All timings in this paper were measured on a system with a clock period of 9.5 ns.

EXAMPLES

SH-wave propagation

We consider wave propagation for the horizontal interface shown in Figure 3. The upper region has *P*-wave and *S*-wave velocities of 2000 m/s and 1200 m/s, respectively, and a density of 1.3 g/cm^3. Lower region *P*-wave and *S*-wave velocities are 4000 m/s and 2000 m/s, respectively, and the density is 1.9 g/cm^3. The source is a directional force acting in the *y* direction. The Ricker wavelet source has a peak frequency of 15 Hz with energy in a range approaching 30 Hz, with a sharp Gaussian shape in space. The model is a cube with 125 points at 20 m spacing in each direction. Figures 4a–4c show three snapshots at different times on three perpendicular planes passing through the source location. *P*-wave and *S*-wave fields are shown in red and blue, respectively. The *S*-wave field on the

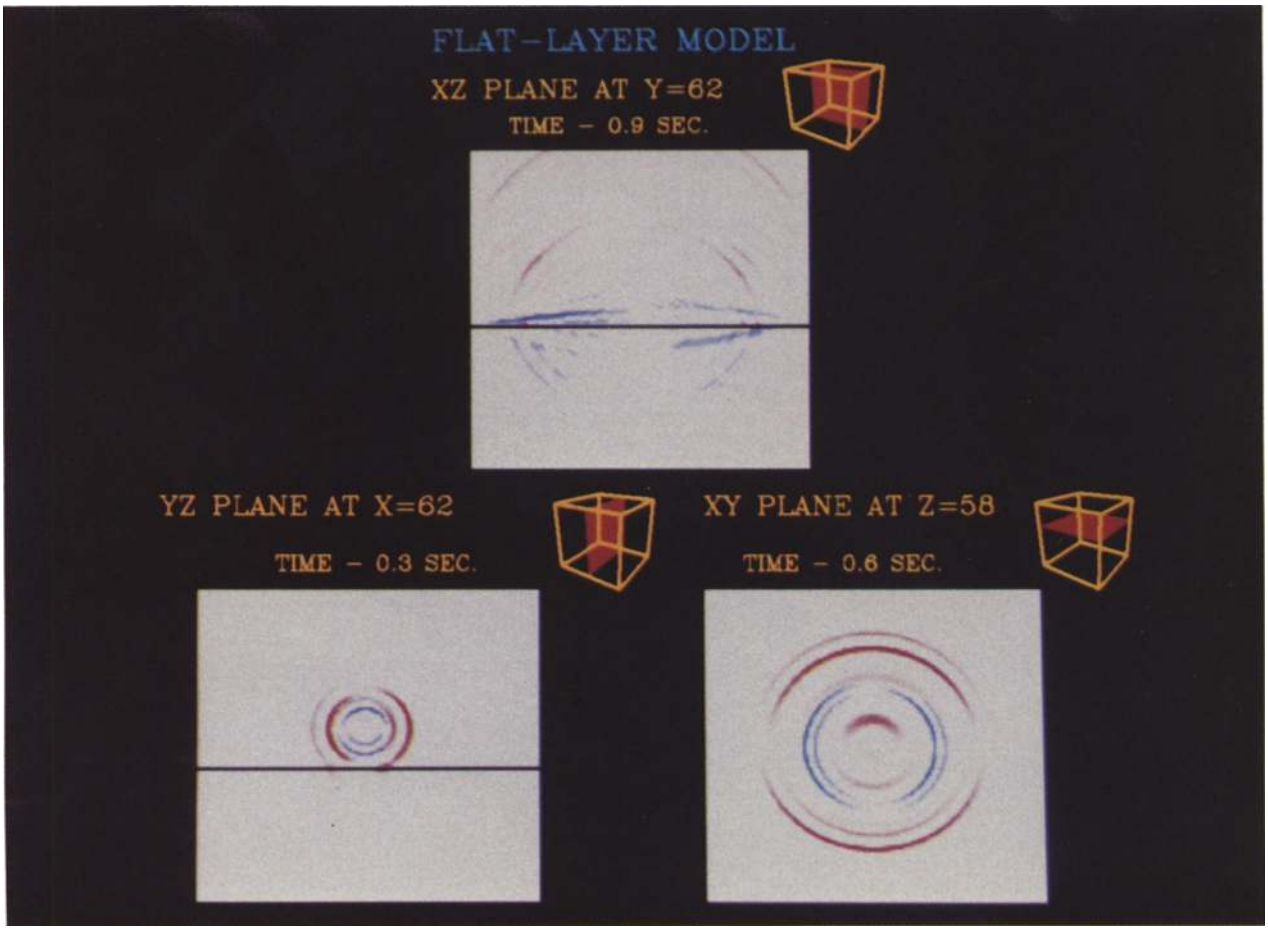

FIG. 4. Plane snapshots for horizontal interface model. *P* waves and *S* waves are shown in red and blue, respectively. The position of each plane within the 3-D volume is shown at the upper right corner.

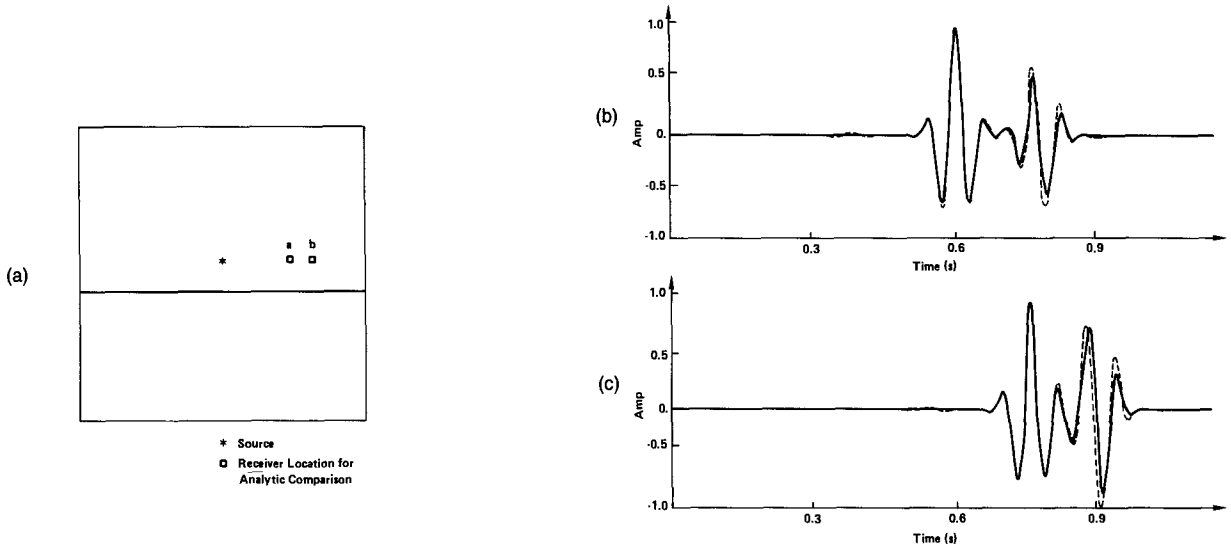

FIG. 5. Horizontal interface model—(a) location of receivers for numerical and analytical comparisons, (b) and (c) numerical (dashed) and analytical (solid) time histories.

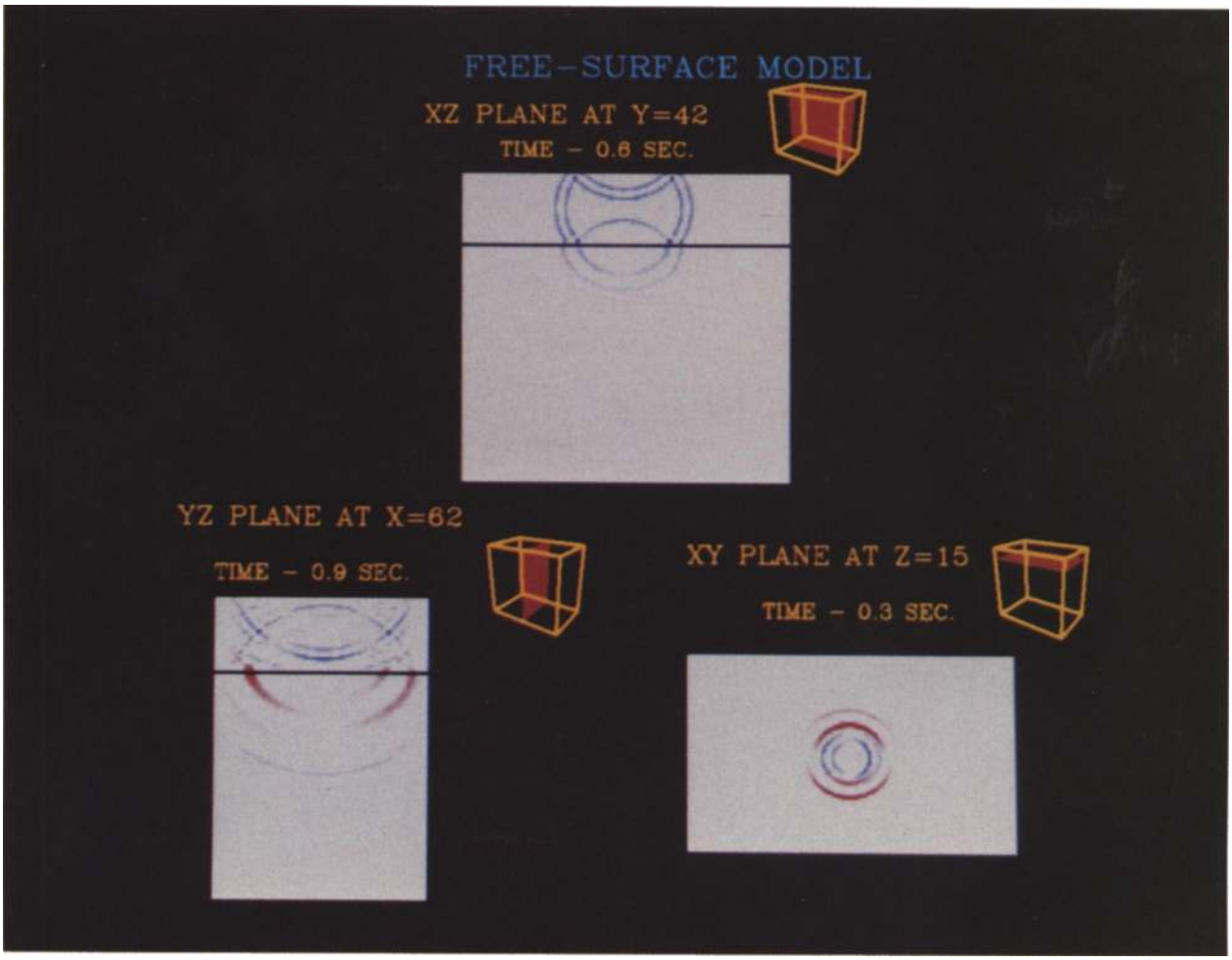

FIG. 6. Plane snapshots for the free-surface model. The position of each plane within the 3-D volume is shown at the upper right corner. Figures 7a–7c correspond to lower left, lower right, and upper snapshots, respectively. Figures 7a and 7b show *P* waves (red) and *S* waves (blue). Figure 7c shows the *y* component of displacement.

xz plane passing through the source location contains SH waves only. Direct P waves and S waves, generated by the source, are represented in the yz plane. The horizontal snapshot (xy plane) shows the two direct waves P (outer red circle) and S, along with two reflected P waves. The first is a PP reflection mixed with the direct S wave, and the second is an SP reflection represented by the inner red circle. At a later time (xz snapshot), P waves in the lower region have already disappeared because of their higher velocity. The y component of displacement (U_y) can be solved analytically on this plane. Two comparisons between numerical U_y results and analytical U_y solutions calculated by the Cagniard-de Hoop method (Aki and Richards, 1980) are shown in Figures 5b and 5c. The locations of the two receivers are shown in Figure 5a. There is good agreement between the numerical results and the analytical solutions for both the direct and reflected waves. The absorbing boundaries appear to perform well, since no appreciable wraparound or side reflections can be determined.

SH-wave propagation with free surface

In this example, we compare numerical results and analytical solutions with a two-layer model underlying a free surface. A spatial grid of 125 × 81 × 125 points is used. The padded or extended region below the grid has 100 points in the z direction. All other physical parameters except the thickness of the upper layer (580 m) are the same as in the previous example (cf., Figure 3). The source (located 280 m above the interface) is also the same as in the previous example. Figures 6a and 6b show P-wave and S-wave fields on two planes passing through the source location. Figure 6c shows the y component of displacement (U_y) in an xz plane perpendicular to the source direction and passing through the source location. The S-wave field in this plane contains SH waves only. Four shear events are clearly represented; the direct wave, the free-surface reflection, the reflection from the material interface in the upper layer, and the wider transmitted wave in the lower layer. The xy snapshot shows the P waves and S waves generated by the source and at a later time. In the yz snapshot, the free-surface reflection, converted phases, reflected waves, and transmitted waves are covering the plane. Four receiver locations on the Figure 6c plane are used for analytical comparisons (see Figure 7a). Five events are observed at each receiver. These are the direct wave, reflected wave, surface multiple, and two reflected multiples. As shown in Figures 7b–7e, the agreement between the numerical results and the Cagniard-de Hoop analytical solutions for the y component of displacement (U_y) is good. The absorbing boundaries appear to have performed well.

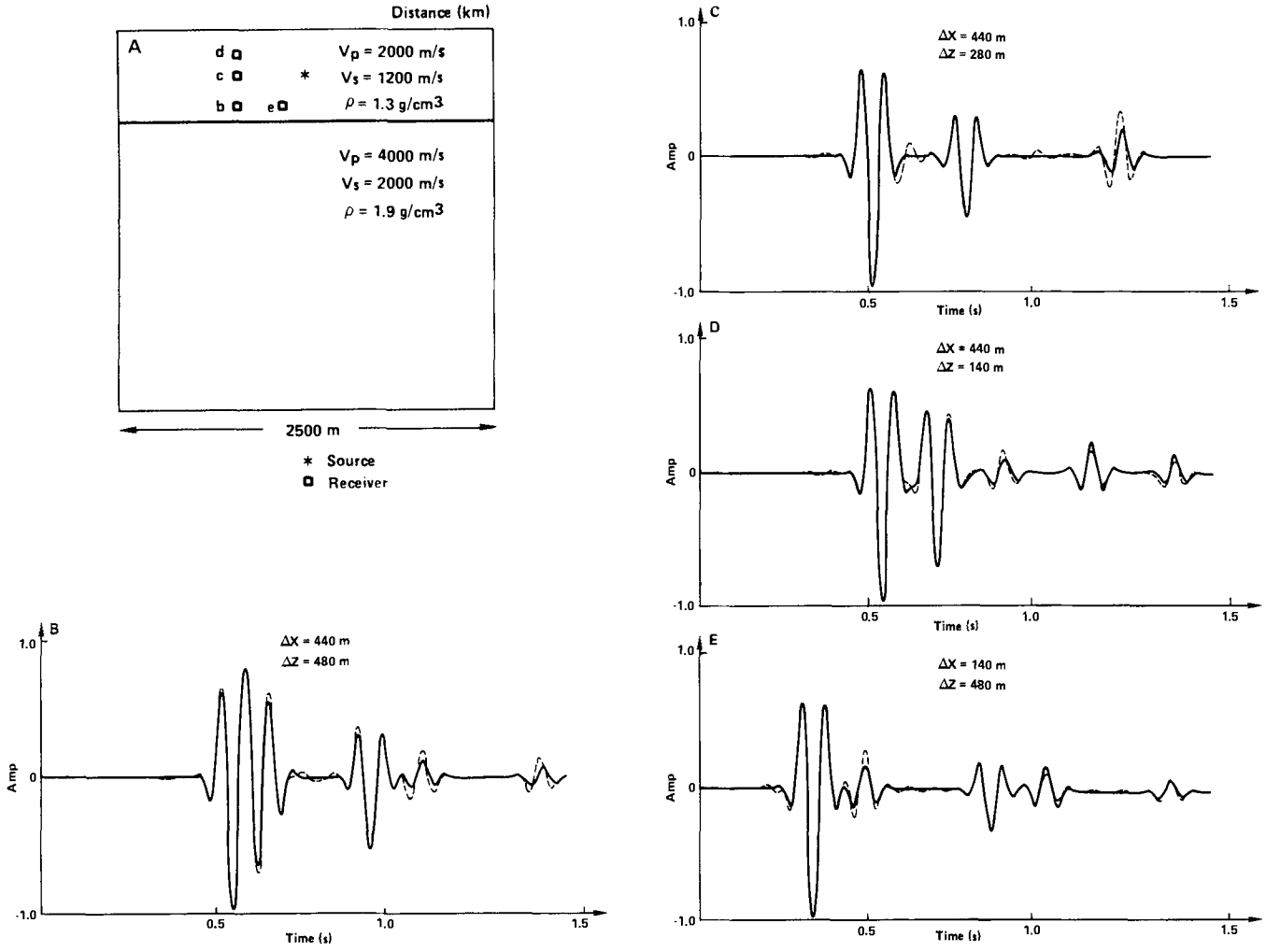

FIG. 7. Free-surface model—(a) location of receivers for numerical and analytical comparisons, (b)–(e) numerical (dashed) and analytical (solid) time histories of the y component of displacement.

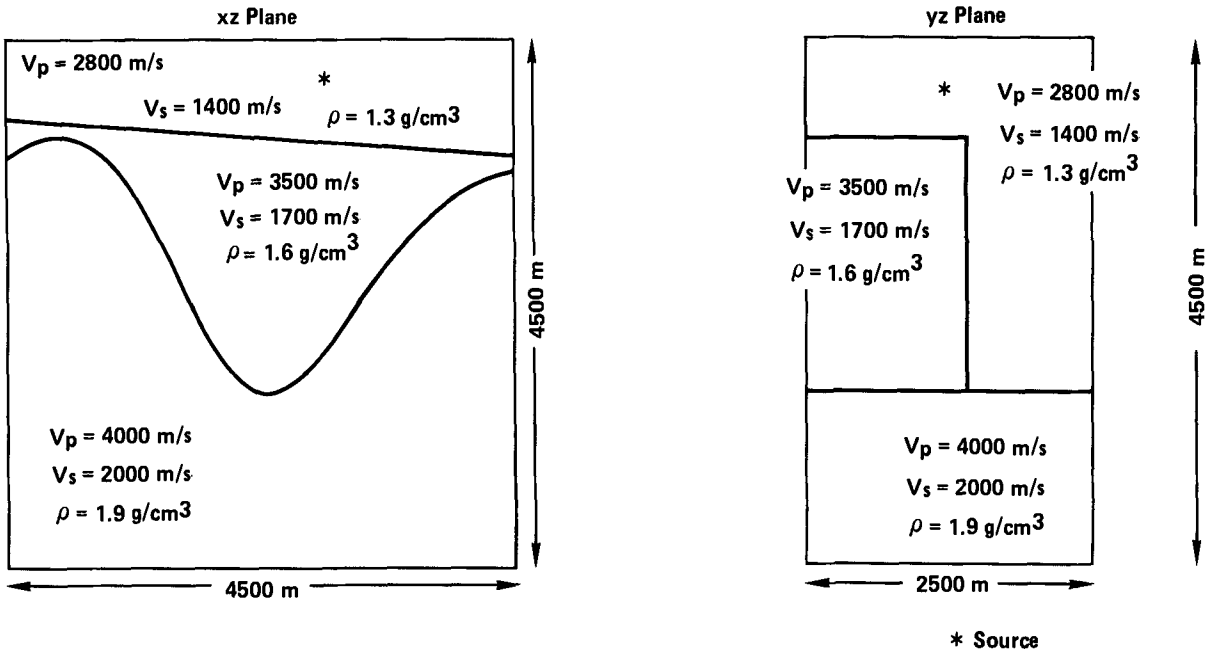

FIG. 8. Syncline model—configuration and physical parameters.

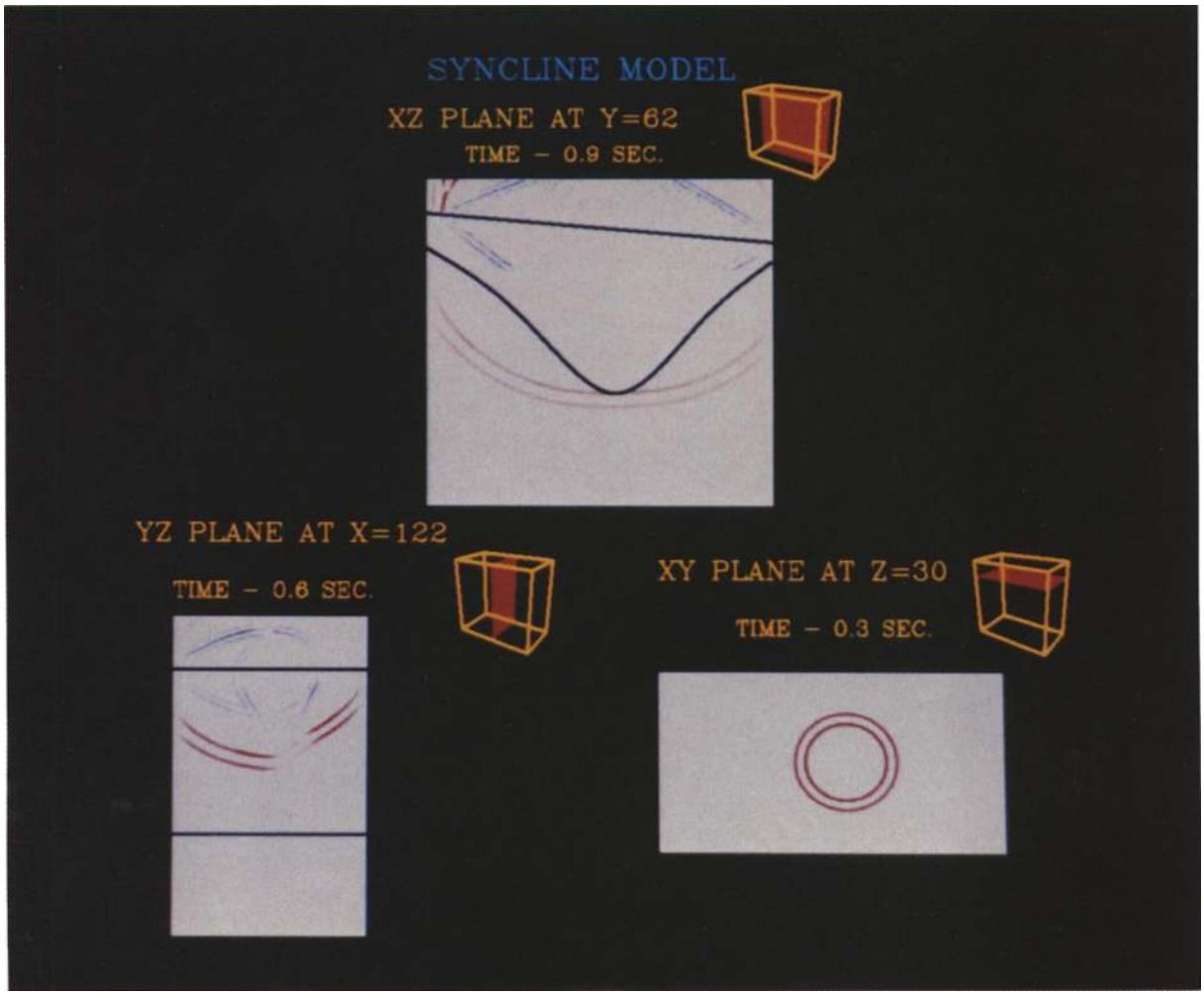

FIG. 9. Plane snapshots for syncline model. *P* waves and *S* waves are shown in red and blue, respectively. The position of each plane within the 3-D volume is shown at the upper right corner. Figures 10a–10c correspond to lower left, lower right, and upper snapshots, respectively.

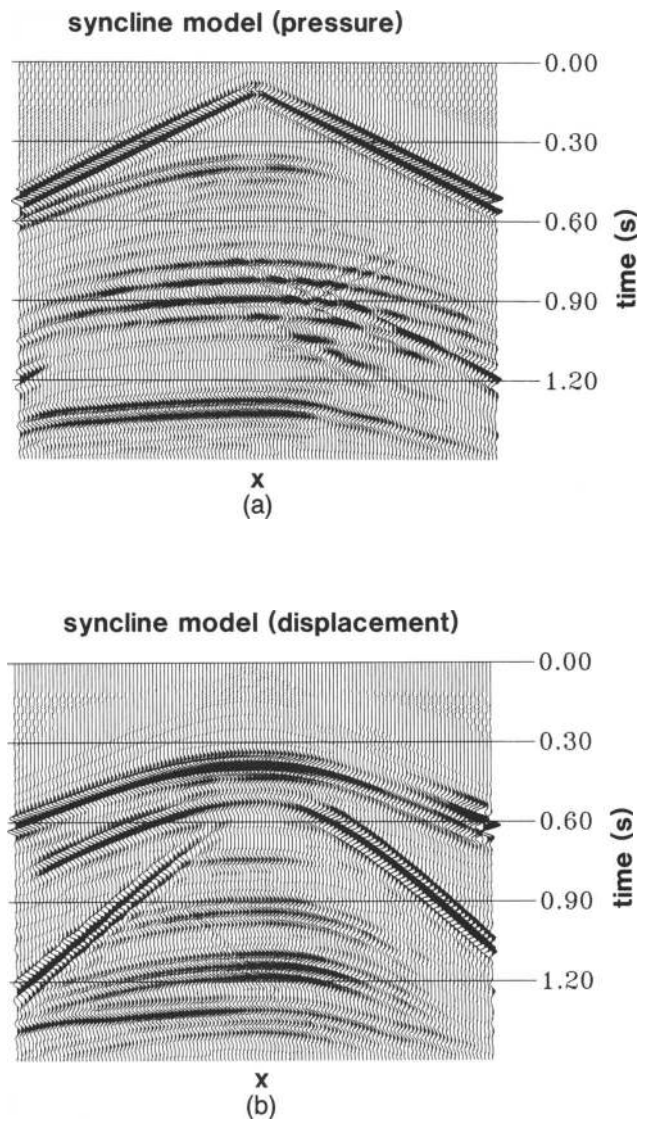

FIG. 10. Syncline model—(a) pressure time section and (b) vertical or z component of displacement time section. Automatic gain control has been applied.

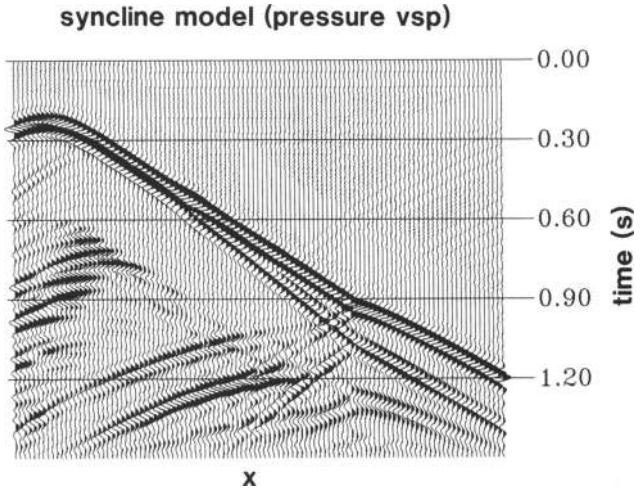

FIG. 11. Syncline model—VSP pressure time section.

Syncline model

This example addresses a more complicated geologic structure. The modeled volume is 4500, 2500, and 4500 m in the x, y, and z directions. A spatial grid of 225 × 125 × 225 points is used with a grid spacing of 20 m. The structure consists of a truncated dipping interface overlying a syncline. A description of the model and its physical parameters is shown in Figure 8. A pressure source with a 35 Hz band-limited Ricker wavelet is used. Figure 9b shows a snapshot taken at an early time on a horizontal plane passing through the source location. This figure shows that the only wave produced by the source was a P wave. Two other snapshots at later times are shown in Figures 9a and 9c. As expected, converted S waves are produced and the wavefront shape is distorted. More information can be obtained by examining the time histories produced by the modeling. For example, Figures 10a and 10b show two time sections measured at 125 receivers along a y-direction line passing through the source location. Figure 10a is the pressure time section, and Figure 10b shows the z component of displacement (U_z) at the same receivers. Some differences between the two sections can easily be noticed. For example, the U_z time section does not include a direct wave but does include some steeply dipping events produced by converted S waves. For another model perspective, Figure 11 shows a VSP time section of pressure using 210 vertical receivers. The 128 million word SSD and dedicated use of the four CPUs of a CRAY X-MP/48 resulted in elapsed or wall-clock time of 4.5 hours for the computation of 1500 time steps.

CONCLUSIONS

For the case of isotropic elastic media, we demonstrate that wave fields for meaningfully sized 3-D models can be computed using existing and proven computer technology. Current computer technology advances, trends, and directions give promise to the role of 3-D modeling.

The Fourier method has the advantage of being a direct solution without compromising material parameter assumptions. Errors are those associated with spatial discretization of dipping and curved structures (the so-called "right solution to the wrong problem"), FFT computation, and time integration of second-order differencing. Acoustic and elastic Fourier forward modeling for variable-density models permits accurate spatial first partial derivative and mixed second partial derivative computation.

Published and publicly disclosed algorithms vary greatly in accuracy and model generalization. Definitions of comparable accuracy are needed to distinguish among the various algorithms. Accuracy can be determined by comparative studies with finite-difference, finite-element, Fourier, and other formulations. An investigation should address issues of source frequency content, grid resolution, time step increments, structure types, and variation of material parameters.

On the basis of experience to date, the Fourier method requires fewer grid points than finite-difference and finite-element methods (Fornberg, 1987). On the other hand, it is well known that finite-difference and many finite-element formulations are computationally more efficient than the Fourier method. Currently, the size of fast, accessible computer memory has the greatest impact on 3-D forward modeling. First, we have to determine if data array storage can fit into

memory; and then we can determine if the required computations are feasible.

Three-dimensional forward modeling accentuates the geophysical community's graphics problem. Our experience to date indicates that outputting time histories at receiver locations on the surface (as in the simulation of a field record) often raises more questions than it answers. Snapshot displays for selected times on various *xz*, *yz*, and *xy* planes can be used for event identification. On the other hand, excessive use of the snapshot capability can present severe computer problems for the on-line storage of snapshots, downloading of large volumes of data from the host system to workstations, and eventual animation. In order to perform 3-D forward modeling on a production or routine basis, the computational expense dictates real-time graphics monitoring to ensure that meaningful results are computed.

ACKNOWLEDGMENTS

This work was partially supported by a 3-D modeling project conducted jointly between the University of Hamburg and Tel-Aviv University under contract 03E 6425A of the BMFT, West Germany, and contract EN3C-0008-D of the European Community Commission. We wish to express our gratitude to Dennis Kuba of Cray Research, Inc. for further optimization of mixed-radix FFT software developed by Clive Temperton, formerly of European Centre for Midrange Weather Forecasting (ECMWF).

REFERENCES

Aki, K. and Richards, P. G., 1980, Quantitative seismology, theory and methods, **1**: W. H. Freeman and Co., chap. 6.

Cerjan, C., Kosloff, R., and Reshef, M., 1985, A nonreflecting boundary condition for discrete acoustic and elastic wave equations: Geophysics, **50**, 705–708.

Fornberg, B., 1987, The pseudospectral method: Comparisons with finite-differences for the elastic wave equation: Geophysics, **52**, 483–501.

Fung, Y. C., 1965, Foundations of solid mechanics: Prentice Hall Inc.

Kosloff, D., and Baysal, E., 1982, Forward modeling by a Fourier method: Geophysics, **47**, 1402–1412.

Kosloff, D., Reshef, M., and Loewenthal, D., 1984, Elastic wave calculation by the Fourier method: Bull., Seis. Soc. Am., **74**, 875–891.

Reshef, M., and Kosloff, D., 1985, Applications of elastic forward modeling to seismic interpretation: Geophysics, **50**, 1266–1272.

Reshef, M., Kosloff, D., Edwards, M., and Hsiung, C., 1988, Three-dimensional acoustic modeling by the Fourier method: Geophysics, **53**, this issue, 1175–1183.

Temperton, C., 1983, Self-sorting mixed-radix fast Fourier transforms: J. Comp. Phys., **52**, 1–23.